Automatic detection of microaneurysms in diabetic retinopathy fundus images using the L*a*b color space

PEDRO J. NAVARRO,[1,*] DIEGO ALONSO,[1] KOSTAS STATHIS[2]

[1] *División de Sistemas e Ingeniería Electrónica, Universidad Politécnica de Cartagena, Campus Muralla del Mar S/N, 30202 Cartagena (SPAIN)*
[2] *Department of Computer Science, Royal Holloway University of London, Egham, TW20 0EX (UK)*
** Corresponding author: pedroj.navarro@upct.es*

Received XX Month XXXX; revised XX Month, XXXX; accepted XX Month XXXX; posted XX Month XXXX (Doc. ID XXXXX); published XX Month XXXX

We develop an automated image processing system for detecting microaneurysm (MA) in diabetic patients. Diabetic retinopathy is one of the main causes of preventable blindness in working-aged diabetic people with the presence of an MA being one of the first signs. We transform the eye fundus images to the L*a*b* color space in order to separately process the L* and a* channels, looking for MAs in each of them. We then fuse the results, and lastly send the MA candidates to a kNN classifier for final assessment. The performance of the method, measured against 50 images with an ophthalmologist's hand-drawn ground-truth, shows high sensitivity (100%) and accuracy (84%), and running times around 10 seconds. This kind of automatic image processing applications are important in order to reduce the burden on the public health system associated to the diagnosis of diabetic retinopathy given the high number of potential patients that need periodic screening. © 2015 Optical Society of America

OCIS codes: *100.2000 Digital image processing; 100.4994 Pattern recognition, image transforms; 110.7410 Wavelets; 150.1135 Algorithms; 170.3880 Medical and biological imaging;*

http://dx.doi.org/10.1364/AO.99.099999

1. Introduction

Diabetes is a disorder of sugar metabolism in the human body, which is unable to maintain the levels of blood glucose within the normal range values (around 4 mmol/L or 72 mg/dL). Diabetes is associated with increased likelihood of suffering systemic vascular complications, including stroke, coronary heart disease, and heart failure. Diabetes can affect the kidney (diabetic nephropathy), heart (diabetic cardiomyopathy), nerves, particularly plantar nerves (diabetic neuropathy), and eye sight (diabetic retinopathy). By 2030, as some studies [1] estimate, 366 million people will suffer diabetes. We focus the work described in this article on the problems caused by diabetes to the eyes.

Although diabetes affects the eyes in many ways (e.g., increasing the risk of cataract), diabetic retinopathy (DR) [2] is the most common and serious ocular complication. Nearly a third of diabetic patients develop DR, which is the main cause of preventable blindness in working-aged people. DR is a silent disease because it goes unnoticed to the patient until the retina has been damaged to a level where treatment is nearly impossible. Therefore, early detection, performed by periodic screening of the eye fundus, is fundamental to treat DR and decrease the probability of suffering blindness at an early age. However, the high number of potential patients and the need for periodic inspection puts a heavy burden on the public health system, and therefore automatic image processing applications are needed to reduce the cost associated to the diagnosis of this illness.

DR is classified into two levels: non-proliferative and proliferative. The latter is the most critical and dangerous, since it is the last stage before blindness. Non-proliferative DR is less critical because there are still ways to maintain its progression under control. Therefore, it is important to be able to detect DR when it is in its first stages, which in turn makes detection more challenging because some of the signs cannot always be obvious after screening. The first microvascular signs of non-proliferative DR are microaneurysms (small ruptures on the capillary wall due to pericyte loss) and hemorrhages (microaneurysm rupture). Signs of a more advanced status are cotton-wool spots (accumulations of axoplasmic debris), hard exudates (lipid deposits), intraretinal microvascular abnormalities (dilated pre-existing capillaries), and venous dilation and beading [2]. See Fig. 1.

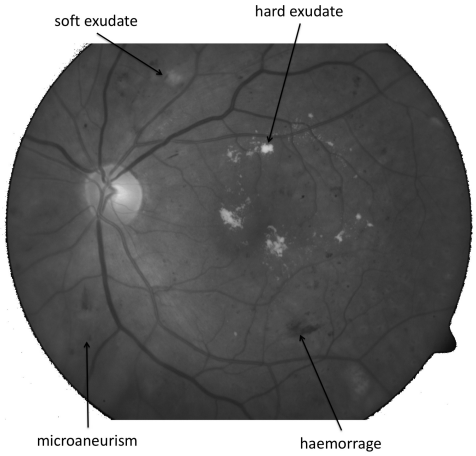

Fig 1. Fundus eye image with the main lesions found in non-proliferative DR

Given the impact DR has over the lifestyle of the patient, previous work in the literature on this topic proposes image processing algorithms with the aim to detect all or some of the lesions caused by diabetes. For example, the article published by Winder et al. [3], reviews 127 methods related to the detection of DR lesions. Nearly all of the methods reviewed employ different algorithms and techniques to detect candidates of being a lesion, and then rely on the use of a classifier or a multilayer perceptron neural network to make the final assessment. The detection of possible candidates varies from method to method, but they can be roughly classified into three groups: (i) those that first detect and erase physiological eye features (like blood vessels, the optic disc and the macula) from the fundus image and then apply filtering algorithms and windowing to detect lesions, (ii) those that employ region growing methods to detect pixels that belong to the same eye feature, and (iii) those that exploit pixel-wise methods that try to classify each pixel in the image and then apply clustering algorithms to detect candidate lesions. Almost all known classifiers have been used: naïve Bayes, k-Nearest Neighbors (kNN), fuzzy C-means, Support Vector Machines (SVM), Mahalanobis and random forest. In some works the classifiers have been trained to distinguish between two classes, while others augment this number up to five classes, depending on their objective. The features extracted from the images in order to train the classifier are of different nature, such as intensity of grey levels, shape (compactness, area, perimeter, etc.), texture (statistical parameters of first and second order), or frequency (Fourier transform).

Following the approach described in Winder et al. [3], more recently there has been a new wave of effort to tackle DR. The work by Welikala et al. [4] employs a dual classification system to detect new vessel in the eye fundus, which is a sign of proliferative DR. The works described in [5] [6] [7] are focused on the detection of exudates and cotton wool lesions, since they can also lead to proliferative DR. proliferative DR detection is also the objective of the work described in [8], where the authors segment blood vessels to try detect neovascularization in the eye. The works by Sopharak et al. [9] and Tang et al. [10] are more related to the work presented in this article, since they specifically target MA and hemorrhage detection. The first method comprises a pre-processing step, exudate and vessel elimination step, mathematical morphology analysis, feature extraction step, and classification of the images by using kNN and Naïve Bayes classifiers, but at the pixel level. They report running times around one minute, sensitivity 85.68%, and specificity 99.99%. The work by Tang et al. [10] use a splat feature classification method in order to detect hemorrhage in eye fundus images. Splats are collection of pixels with similar color and spatial location. They generate the splats by applying several algorithms, then extract some features and use a kNN classifier to label the splats. They report a sensitivity of 93% and specificity of 66%. After the training process, it takes the classifier no more than 15s to assign splat labels to one image on a computer equipped with a two-core Intel X9650 processor running at 3.00 GHz.

It is also worth highlighting totally new approaches to tackle DR diagnosis. Such approaches rely completely on machine learning and statistical techniques in that they do not apply "classical" computer vision algorithms, but rather so-called ensemble methods for classification. In these approaches, a set of components is generated from training data and each component casts a vote for the predicted label of a given object. Casanova et al. [11] describe the application of random forests algorithms, which are highly nonlinear approaches specially suited for high-dimensional data, to classify fundus images. Tang et al. [12] describe an evolutionary approach simulating how humans recognize objects: they obtain a general impression first, and concentrate on concrete details later. The system they propose is based on a set of ensembles of a large number of classifiers for different image contents, which are then optimized by the application of evolutionary algorithms. A Hidden Markov Model, also generated by evolutionary computation, is used to keep the visual context. The information generated by the optimized classifiers and context models is then fused together to determine the image content. The average sensitivity and specificity results are above 90% in all tested configurations. However, the performance of the software is still slow, with running times ranging from 10 to 25 minutes in an Intel Core i7 with 8GB RAM. Roychowdhury et al. [13] describe a system that employs two hierarchies of classifiers to perform lesion classification (hemorrhages and MA, hard exudates and cotton wools), which enables them to reduce the number of features that must be processed.

A problem with the works described above is the overreliance on analyzing information contained in one channel only [3], normally the green channel (RGB) of the fundus image, since this channel contains the vast majority of the information regarding anatomical structures. As such, the information is heavily concentrated in the G-channel [3], what hinders the segmentation process and makes it computationally expensive, with running times often in the order of minutes. The election of the optimum color space for processing digital images is a crucial step in image processing, since algorithms are then applied to process the information contained in just one channel of the image. Therefore, the election of a channel with "the optimal amount of information" for identifying lesions related to DR has a major impact on the performance and complexity of the algorithms, as well as on their execution time.

In this work we explore the use of the L*a*b color space [14] to prevent the problems associated with the correlation that exists between the information contained in the RGB channels. In existing works, only the methods by Niemeijer et al. [15], Roychowdhury et al. [13], and Thomas et al. [6] look at other color spaces than RGB, being HSI (Hue, Saturation, Intensity) the chosen one. The first two methods only use the I (Intensity) channel to extract image features for the classification step, while only the work by Thomas et al. [6] employ the I channel throughout the whole process. In the work by Tang et al. [10], color within each splat is extracted in RGB color space and dark-bright (db), red-green (rg), and blue-yellow (by) opponency images, so they also employ data from other color space.

The main hypothesis of our work is that the joint processing of the L* and a* image channels and the subsequent fusion of its results can lead to better results and faster algorithms. In the set of images we have examined from the considered database, MESSIDOR [16], we have realized that the information related to anatomical structures, and particularly MAs, is distributed between channels L* and a* instead of being concentrated in just one channel. We test this hypothesis with the development of an automatic system for the detection of MA candidates, since they are the earliest clinical sign of non-proliferative DR and also one of the hardest lesions to detect, given that they appear as small (from 12 to 100 μm, although only those larger than 30 μm are visible ophthalmoscopically), red dots in the superficial retinal layers (see Fig. 1).

Once the MA candidates have been selected, we apply the wavelet transformation to them to extract the features that are afterwards sent to a kNN classifier in order to finally determine whether the candidate image is an MA. The use of the wavelet transform for texture characterization is well established in pattern matching analysis [17][18], but only the work by Quellec et al. [19] apply it in order to detect MA. However, their method relies on template-matching in the wavelet domain for detecting MA, which is different from our approach. They report a sensitivity and a positive predictive value of 89% for the detection of microaneurysms in 120 retinal images of several imaging modalities.

The organization of this paper is as follows. Section 2 describes details of the methodology. Section 3 presents the experimental evaluation. Finally, a discussion and conclusion are given in section 4.

2. Materials and Methods

In this work we assume that an image is sampled, generating a digital image $f(x, y)$ with 'M' rows and 'N' columns [20], according to the resolution of the capturing device. Fundus digital image of the eye are sampled in three channels, corresponding to the RGB space color, and

therefore the values of the coordinates (x, y) now become discrete quantities. We denote with a super index each channel of the image $f^c(x,y), \forall\ c = R, G, B, L, a, b$. 1 byte is employed to store the color value of each channel; therefore, the range goes between 0-255. Image transformations (T_i) are represented as $T_i[f^c(x,y)]$, without indicating the channel since transformations are normally channel-independent.

The method proposed in this work for the automatic detection of MA is composed of three steps (see Fig. 2):

1. *Pre-processing*. The lack of uniformity and the changing lighting conditions found in the database of fundus images adds complexity to the automatic detection and evaluation of the DR degree and lesion kind. Blurred eye borders, very dark or light areas, and reflections are some examples of the kind of defects found on images. These defects are normally due to wrong patient placing, changing conditions on the equipment over time and different parameters configuration (such as channel gain, exposure time and pre-processing method). Therefore, images must be normalized before further algorithms can be applied to process them.
2. *Selection of candidates of being MA*. Thresholding algorithms are used to separate objects of interest (MA candidates) from the image background in channels L* and a*. Then, candidates found in both channels are fused into a single image, from which shape-related features are computed in order to select the final set of MA candidates, which will be checked by a classifier in the third step.
3. *Classification of candidates*. The wavelet transformation is then applied to MA candidates in order to extract a set of features that are later used by a kNN classifier to detect whether the candidate is an MA.

The remaining of this section is devoted to describe all the steps of the method and the algorithms applied in the same order as they appear in Fig. 2.

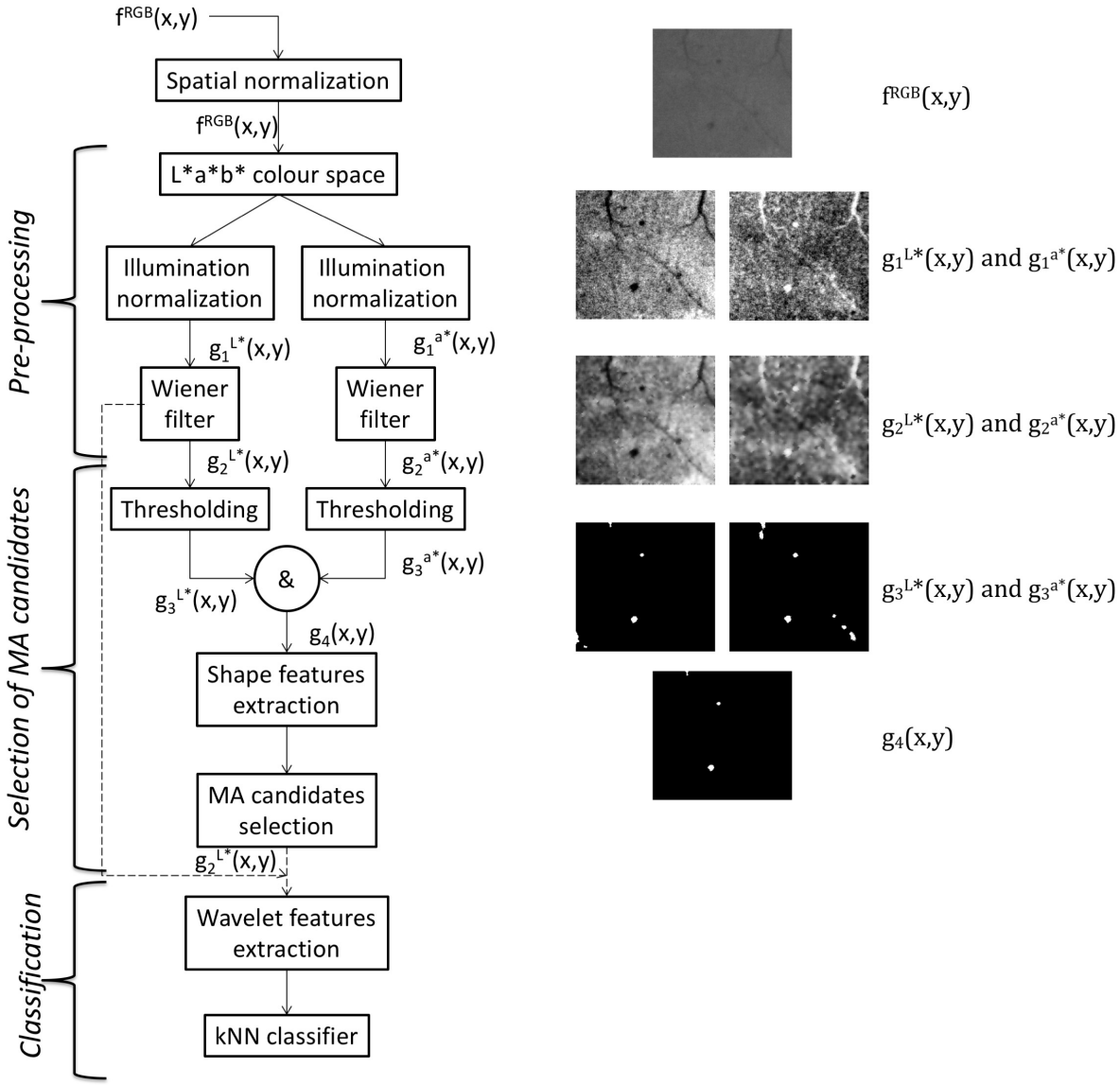

Fig 2. Proposed method for MA detection based on the data fusion of L* and a* channels (left). Resulting images after each step of the method (right).

A. Spatial Normalization

The objective of this step is to homogenize the geometric values related to objects appearing in the image, such as areas, distances and volumes. We apply the method proposed in [7], which mainly employs the diameter (D) of the Field of View as a reference to normalize all spatial measurements performed over the digital image. The segmentation of the field of view is an easy task that can be performed by applying a simple thresholding algorithm [21], since the area outside the eye is completely black in the images. This kind of algorithm calculates a threshold value 't' that separates objects from the background in an image. We use the simplest one, called binarize, which only considers two possible values: object and background. We apply the thresholding algorithm defined in Eq. 1 to the red channel of the input image to segment the eye.

$$t = \Xi - 2,5 \cdot X, \qquad (1)$$

Ξ is the mean, X the standard deviation, and X^2 the variance:

$$\Xi = \frac{1}{N \cdot M} \sum_{i=1,j=1}^{N,M} f(i,j)$$

$$X^2 = \frac{1}{N \cdot M} \sum_{i=1,j=1}^{N,M} (f(i,j) - \Xi)^2$$

Once the image has been segmented, Eq. 2 allows us to estimate 'D'.

$$D = \frac{dAM + dAm}{2} \qquad (2)$$

Where *dAM* and *dAm* are the values of the largest and smallest diameters of the ellipse that defines the segmented eye. Given 'D', the size of the following anatomical structures are empirically estimated:

- d1 is the average diameter of the optic disc, d1 = D/5;
- d2: is the maximum width of vessels, d2 =D/74;
- d3: is the size of the smallest lesions, d3=D/99.

B. L*a*b* Color Space

A color space is a mathematical representation of a set of colors. The most popular ones are RGB (computer graphics), YUV and YCbCr (video systems), and CMYK (professional color printing). Other color spaces such as HSI and HSV aim at representing, in a more intuitive way, the notions of hue, saturation, and brightness. The CIELAB [14] color space, also known as L*a*b*, represents luminosity in channel L*, while channels a* and b* contain color data: information from red and green in channel a*, and information from blue and yellow in channel b*. This color space is able to model all colors from the visible specter as well as colors outside of it. Though L*a*b* allows for a more accurate representation of colors, it is not however as much used as RGB, YUV or HSI.

Due to the fact that MA are anatomically defined as red dots in the superficial retinal layers, we selected channels L* and a* in order to detect them. This election has reduced the computational complexity of the segmentation algorithm and simplified the classification of the MA candidates in the last step of the proposed method.

C. Illumination normalization

In order to compensate the lack of illumination uniformity in some images due to the problems already mentioned, we compensate its contrast by applying an illumination normalization algorithm (see Eq. 3). This algorithm performs a linear transformation in the spatial domain to make MAs stand out from the background.

$$g_1^c(x,y) = T_1[f^c(x,y)] \; \forall \; c = L^*, a^* \qquad (3)$$

$$m = min(f)$$

$$M = max(f)$$

As shown in Fig. 2, this normalization process enhances the image contrast, easing the detection of candidate of being MAs. Spectral features of MAs are amplified in channels L* and a* but in reverse: MA candidates are bright in channel L* and dark in a*.

D. Wiener Filter

The objective of the filtering step is to denoise the texture of the background while keeping the values of MA candidates. We have applied a Wiener filter [22] (see Eq. 4), which is based on statistics estimations from the local neighborhood (of size 'n' by 'm' pixels) of each image pixel. The results of applying the filter to each channel are shown in Fig. 2.

$$g_2^c(x,y) = T_2[g_1^c(x,y)] \; \forall \; c = L^*, a^* \qquad (4)$$

$$g_2^c(x,y) = \mu(x,y) + \frac{\sigma(x,y)^2 - \zeta^2}{\sigma(x,y)^2}(g_1^c(x,y) - \mu(x,y)), \text{ where:}$$

$$\mu(x,y) = \frac{1}{n \cdot m} \sum_{i=y-\lfloor \frac{m}{2} \rfloor}^{i=y+\lfloor \frac{m}{2} \rfloor} \sum_{j=x-\lfloor \frac{n}{2} \rfloor}^{j=x+\lfloor \frac{n}{2} \rfloor} g_1^c(i,j)$$

$$\sigma(x,y)^2 = \frac{1}{n \cdot m} \sum_{i=y-\lfloor \frac{m}{2} \rfloor}^{i=y+\lfloor \frac{m}{2} \rfloor} \sum_{j=x-\lfloor \frac{n}{2} \rfloor}^{j=x+\lfloor \frac{n}{2} \rfloor} g_1^c(i,j) - \mu(x,y)^2$$

$$\zeta^2 = \frac{1}{Z} \sum_{i=1}^{Z} \sigma_i^2,$$

where Z is the total number of considered neighborhoods.

E. Thresholding method

The pre-processing phase has separated in the extreme positions of the histogram the objects in the image, where the thresholding algorithm shown in Eq. 5 can now be applied to binarize the image. The constants appearing in the equation have been selected empirically.

$$g_3^c(x,y) = T_3[g_2^c(x,y)] \; \forall \; c = L^*, a^* \qquad (5)$$

$$t^L = \mu^L - 2(\sigma^L)^2, \quad t^a = \mu^a + 2(\sigma^a)^2$$

$$g_3^L(x,y): \begin{cases} g_2^L(x,y) > t^L \rightarrow 1 \\ otherwise \rightarrow 0 \end{cases}$$

$$g_3^a(x,y): \begin{cases} g_2^a(x,y) > t^a \rightarrow 0 \\ otherwise \rightarrow 1 \end{cases}$$

Where μ^c, σ^c are the mean and variance of channel 'c' of the image. We finally merge the images generated from channels L* and a* by applying an AND operator, as shown in Eq. 6. The results of applying these two steps are shown in Fig. 2.

$$g_4(x,y) = g_3^L(x,y) \; AND \; g_3^a(x,y) \qquad (6)$$

F. Extraction of Shape Features

In this step the 'nO' objects (set of adjacent pixels with value '1') found in the merged image $g_4(x,y)$ are labeled and stored in $OL = \{ol_1, \dots, ol_{nO}\}$. The following 'nf' shape features are then calculated on each object in the set. Eq. 7 is afterwards applied in order to determine whether it is finally a MA candidate or can be discarded.

(f_1) Area: number of pixels inside the object.

(f_2) Eccentricity: the ratio between the foci of the ellipse and its major axis length. The value is between 0 (circle) and 1 (line segment).

(f_3) Centre of mass of the object.

$$OL_{jj} \in MA \Leftrightarrow \begin{cases} d_3 < \sqrt{\dfrac{4 * F(jj,1)}{\pi}} \leq d_4 \\ AND \\ F(jj,2) < k_2 \end{cases} \quad (7)$$

$$\forall\, jj = 1, \dots, nO$$

where d4=k_1 ·d_3 , size of biggest lesion

$$where\ F(jj,ii) = \begin{bmatrix} f_{1,1} & \cdots & f_{1,nf} \\ \vdots & \ddots & \vdots \\ f_{jj,1} & \cdots & f_{nO,nf} \end{bmatrix}$$

$$\forall\, jj = 1, \dots, nO \quad \forall\, ii = 1, \dots, nf$$

Where MA is the set of possible candidates, and k_1 and k_2 are constants empirically obtained defining the maximum diameter of an MA (5) and its minimum elongation (0,35). The centers of mass of the MA candidates are employed by the classification step to determine the region of interest that should be analyzed. The size 's' of such region of image g_3^{L*} is determined by Eq. 8.

$$s = 2 \cdot d_3 \cdot k_1 \quad (8)$$

G. Texture classification

Once the MA candidates have been identified, the next step is pattern matching. We address this problem from the point of view of texture classification, which is usually divided into two steps: feature extraction and classification.

1. Feature extraction with the wavelet transform

The characterizations of texture using the wavelet transform is well established in pattern matching analysis [17][18][23][24]. Discrete Wavelet Transformation (DWT) generates a set of values formed by the "wavelet coefficients". The main characteristics of the wavelet transformation are that (i) it can be used for accurately deconstructing and reconstructing finite, non-periodic and/or non-stationary signals (in fact, the JPEG 2000 image format employs this transformation to reduce file size by deleting high-frequency information from the original image), and (ii) unlike the Fourier transform, the wavelet provides both frequency and space information, which allows to find not only a given frequency, but also the position in the image where the frequency appears.

The wavelet transform applied in image processing analysis (2D-DWT) decomposes the image by applying a sequence of functions: a scaling function ϕ^{LL} and shifted and dilated functions $\psi^{LH}, \psi^{HL}, \psi^{HH}$ constructed/derived from mother wavelet functions. There are several wavelet mother functions that can be employed, like Haar, Daubechies, Coiflet, Meyer, Morlet, and Bior, depending on the concrete texture to be identified [25] [26].

2D-DWT is implemented by filter banks where a low-pass (LPF) and a high-pass (HPF) filters are sequentially applied to the rows and columns of the original image $f(x,y) = f_{LL}^{(0)}$. In the first decomposition level, the filter banks generate four sub-bands, $f_{LL}^{(1)}$, $f_{LH}^{(1)}$, $f_{HL}^{(1)}$, and $f_{HH}^{(1)}$. In the j-th decomposition level, $f_{LL}^{(j)}$ contains a scaled representation of the original image called "approximation", while LH, HL and LL represent the horizontal, vertical and diagonal details of the image. The process is applied to LL sub-band recursively. Fig. 3 shows the pyramid algorithm of wavelet transform in the first decomposition level. A complete description of its application in both the direct and reverse directions can be found in [20]. Fig. 4 shows four levels of decomposition of 2D-DWT over a MA image.

The textural properties of each of the sub-bands are computed afterwards from a set of grey-level co-occurrence matrices (GLCM) [27], each of which contains a set of second order statistical measurements related to texture. A $GLCM_{d,\theta}$ matrix is defined with two parameters: the distance 'd' and the angle 'θ' applied to compute each position of the matrix $GLCM_{d,\theta}(i,j)$, which contain the number of pixels with grey level 'j' found at distance 'd', angle 'θ' of a pixel with grey level 'i'. That is, a joint occurrence of both grey levels. In this work, we have calculated four such matrices: $GLCM_{1,0}$, $GLCM_{1,45}$, $GLCM_{1,90}$, and $GLCM_{1,135}$.

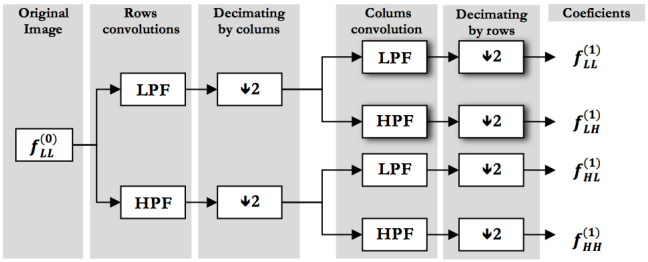

Fig 3. First level of direct 2D-DWT decomposition

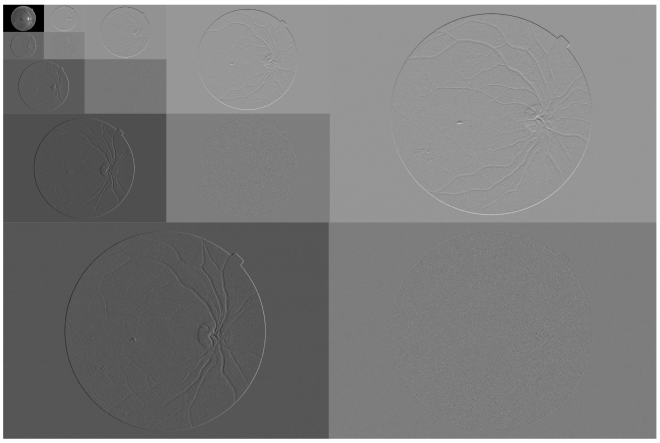

Fig 4. Four decomposition levels wavelet with Haar mother-function

We have selected the following 8 features from each of the GLCM matrices [27]: angular second moment (f_1), contrast (f_2), correlation (f_3), inverse different moment (f_5), entropy (f_9), information measures of correlation (f_{12}, f_{13}), and maximal correlation coefficient (f_{14}). In total, each MA candidate sub-image is characterized by 256 textural features: 8 features from each of the 4 GLCM computed for each of the 4 sub-bands obtained by applying 2 levels of wavelet decomposition using the Haar mother function.

2. kNN Classifier

We have trained a kNN classifier to finally discriminate MA from non-MA (NMA) candidates. We also tested Naïve Bayes and SVM classifiers, but kNN was the one that gave us better results, though the numbers were very close for the three of them. kNN is a non-parametric method for classifying objects in a multi-dimensional space. Once trained, it classifies a new object according to the labels of the k-nearest objects.

The kNN classifier has been trained with regions extracted from 100 images taken from the MESSIDOR database [16]. We selected this database since it provides images with a very high quality (high resolution in TIFF format) and is also well-known in the DR literature. 512 regions of interest have been extracted from these images, containing representative instances of the anatomical structures present in the DR problem (see Fig. 5). The classifier has been trained to recognize two classes: MA and NMA as follows:

- A region is classified as MA if it contains at least one MA. 88 out of the 512 selected training regions belong to this group.
- The remaining 424 regions are classified as NMA, and they contain eye background (BK, 200 region images), hard and soft exudates (EX, 76 region images), hemorrhages (EX, 48 region images) or blood vessels (VE, 100 region images).

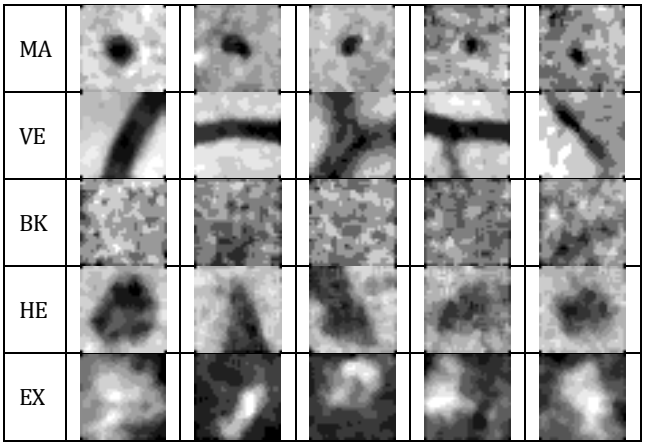

Fig 5. Some of the image regions selected for training the classifier.

3. Results and Discussion

In this section we evaluate the results of training the kNN classifier with a leave-one-out cross-validation method, as well as the results obtained after applying the proposed method to a set of fifty eye fundus images from the MESSIDOR database.

The performance of machine learning algorithms, a kNN classifier in our case, is normally evaluated by means of the Receiver Operating Characteristic (ROC) curve. The ROC curve is created by comparing the rate of true positives (sensitivity, see Eq. 9) versus the rate of false positives (1-specificity, see Eq. 10) at various threshold levels. The ROC curve, shown in Fig. 6, allows comparing the results with other works. The Area Under the Curve (AUC) is 0,9784. These results are very satisfactory from the point of view of MA detection. It must be highlighted that an increase in sensitivity is accompanied by a decrease in specificity.

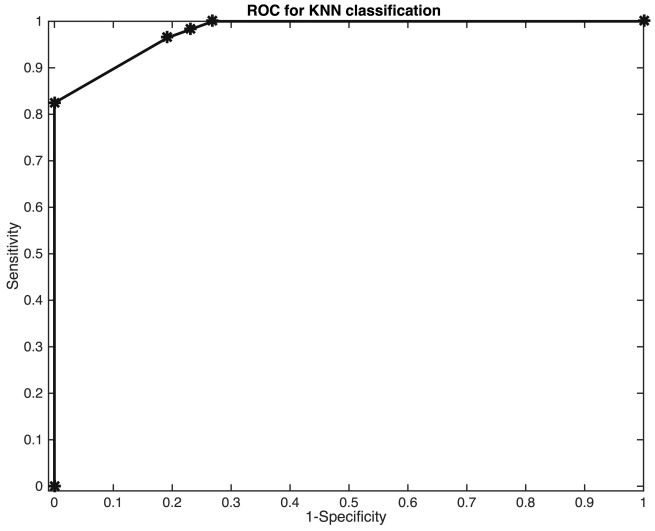

Fig 6. ROC curve for the kNN classifier

Fifty eye fundus images from the MESSIDOR database have been used to test the method. MAs have been hand-drawn by an ophthalmologist, creating a set of 50 ground-truth images. Ten of those images had MAs in them, thirty-five in total. The results of the proposed method are summarized in Table 1. Unlike other works, we focus the validation on the correct detection of MAs in the images and not in the count of pixels. As can be seen in the table, only one MA was not correctly detected in the ten images with DR, which is a very good result, showing that the method has high accuracy. However, the ratio of false negatives is still high since the method has been designed to detect all structures that look like an MA. Sensitivity (see Eq. 9), specificity (see Eq. 10), precision (see Eq. 11), and accuracy (see Eq. 12) are 100%, 80%, 55%, and 84%, respectively. From the point of view of a DR diagnosis assistance system, and taking into account that MAs are difficult to detect (from 12 to 100 μm), it is preferable that the system marks all MA candidates for the ophthalmologist to review.

Table 1. Summary of the performance of the described method.

	Set of 10 images with 35 MA		Set of 40 images without MA	
	correctly	not correctly	correctly	not correctly
Images detected	10	0	32	8
MA detected	34	1	0	16

$$Sensitivity = \frac{TP}{TP + FN} \quad (9)$$

$$Specificity = \frac{TN}{TN + FP} \quad (10)$$

$$Precision = \frac{TP}{TP + FP} \quad (11)$$

$$Accuracy = \frac{TP + TN}{TN + FP + TP + FN} \quad (12)$$

The software has been executed on a PC with an i7 2.6 GHz CPU, 8 Gb RAM using the MATLAB program. The running time per image (2304×1536 pixels) of our proposed method range from 7 to 16 seconds, depending on the number of candidates to be examined.

Figure 7 shows some results of the application of the proposed method to some testing images. The original test images from the MESSIDOR database are shown in the first column. The MA candidates obtained after merging the results of processing the L* and a* channels are shown marked with a blue square in the second column. The decision of the kNN classifier is shown in the third column: candidates marked with a yellow square have been classified as NMA, while those marked with a green square are classified as MA.

Figure 7 also shows some interesting features of the L*a*b* color space, like the fact that we do not have to detect and eliminate the optic disc (first row) from the image, and that exudates (second row) are also filtered out and do not interfere with the detection of an MA. The three remaining rows show that blood vessel are challenging. When an MA is very close to a blood vessel, the kNN classifier normally classifies the region as NMA, while vessel intersections and bifurcations are also normally part of the candidates set. This is the main reason why we have a high ratio of false negatives. Therefore, the first enhancement to improve the results is to add a blood vessel segmentation step to eliminate them from the image, as described for instance in [4] [6] [7] [8], to mention but a few.

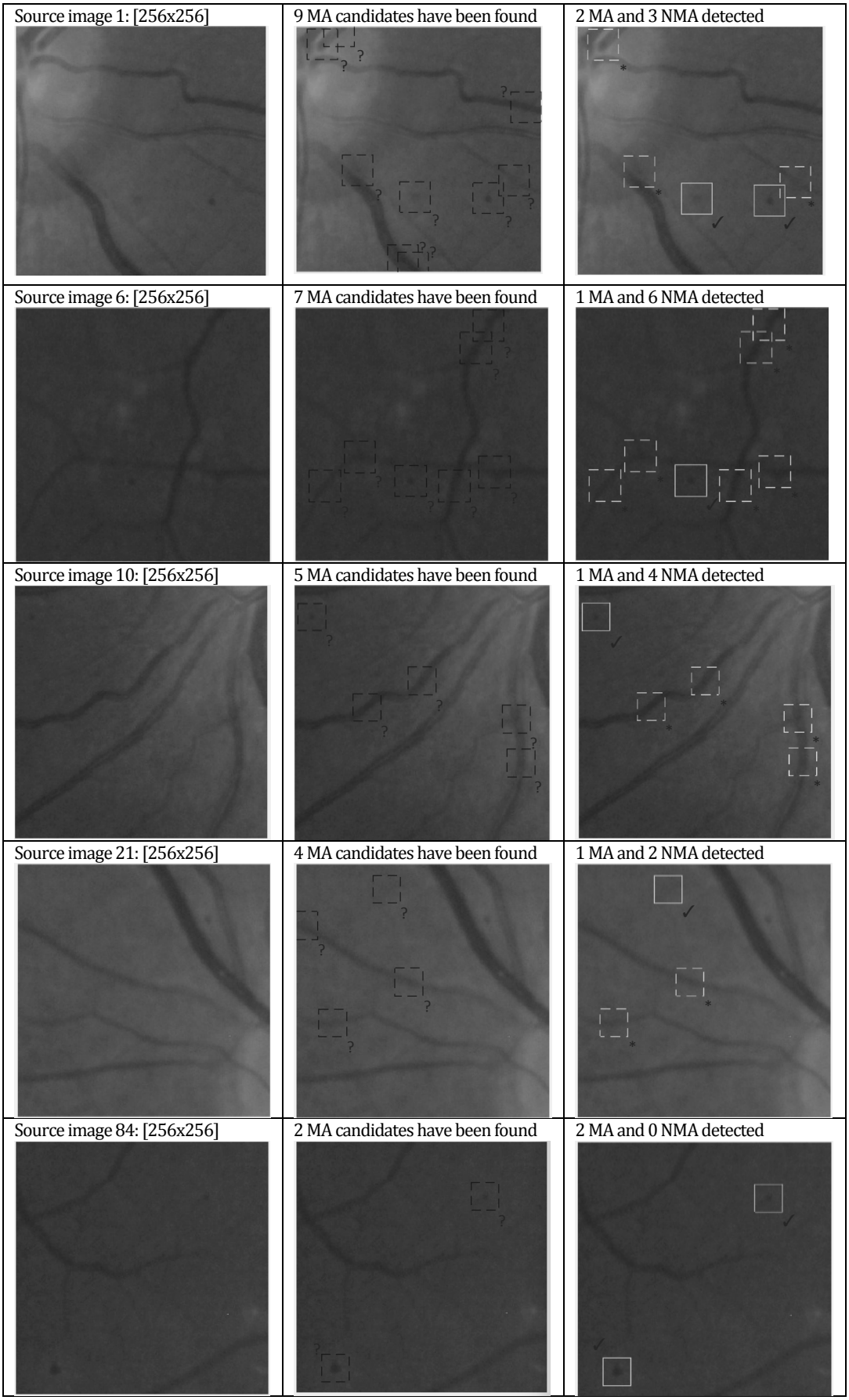

Fig. 7. Some results from the testing images. Left column: original image, middle column: MA candidates marked with a ? square, right column: candidate classification as MA (✓square) or NMA (*square)

Figures 8 and 9 compare the results obtained in the work described in this article, in terms of sensitivity and specificity of the developed computer vision algorithms, with the results of other, similar works. Specifically, Figure 8 compares our results with other works that also process images from the MESSIDOR database, but that tackle the problem of diagnosing the DR status, not only the MA detection. Data extracted from [13]. All reported results of the reviewed methods achieve higher sensitivity but lower specificity than our work. They also show lower AUC, which measures how well the test separates the images in the group being tested. Figure 9, on the other hand, compares our results with other works that focus exclusively on the detection of MA and hemorrhages in images coming from different sources, not exclusively MESSIDOR. Data extracted from [3]. In this case, the methods obtain similar results. Unfortunately, no report is made about running times to further compare the approaches.

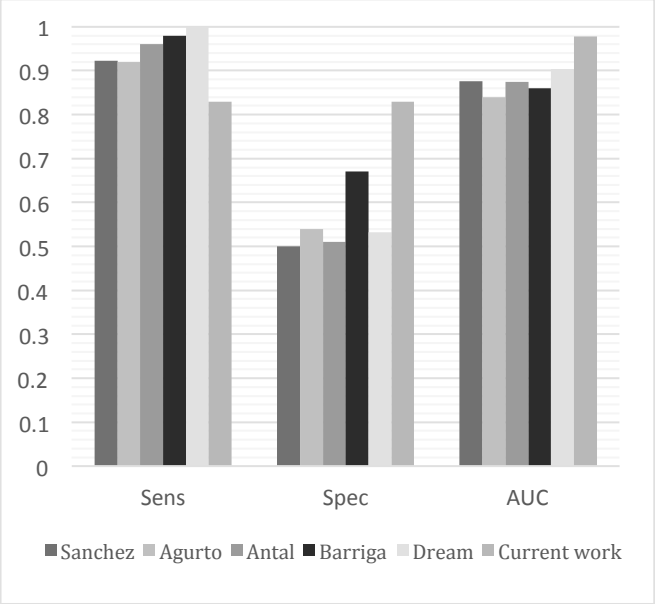

Fig 8. Comparison with other works that diagnose DR status and that use the MESSIDOR database. Data extracted from [13].

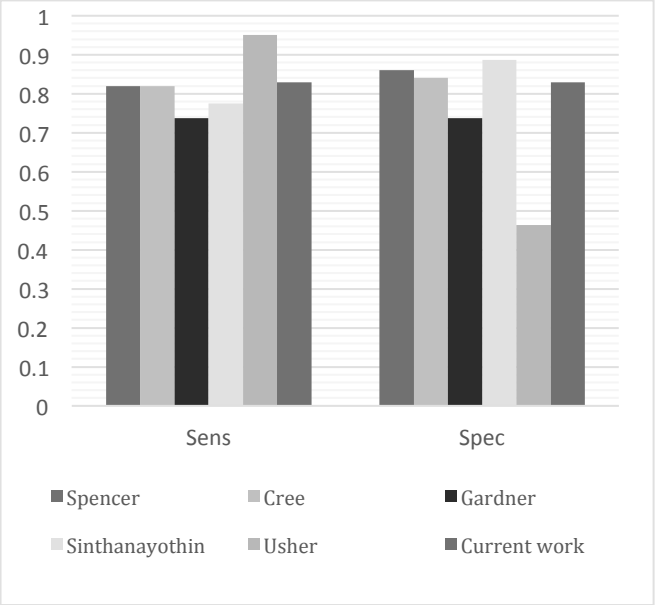

Fig 9. Comparison with other works that detect MA and hemorrhage only, from different source images. Data extracted from [3].

4. Conclusions

In this article, we proposed a method for detecting signs of microaneurysm (MA), one of the first signs of non-proliferative diabetic retinopathy, by analyzing eye fundus images from the publicly available MESSIDOR database. Unlike other works available in the literature, we focused on the L*a*b* color space, processing the information of the L* and a* channels, and then merging the results of both channels in order to quickly identify MA candidates. After that, we apply the wavelet transform to the candidates in order to obtain a set of 256 features that are afterwards given to a kNN classifier to classify the candidates as MA or non-MA.

The proposed method for MA detection is effective, yet fast and simple, intended to help ophthalmologists detect the symptoms of DR more easily and accurately in the periodic screening processes. Though we currently detect MA candidates only, we plan to extend this work to identify other lesions. The performance of the method, measured against 50 images with an ophthalmologist's hand-drawn ground-truth, shows high sensitivity, specificity and accuracy, all above 80%. The running times range from 7 to 16 seconds in an Intel i7 processor, depending on the number of candidates found.

Regarding future work, we will continue working with the idea of processing the image in different color spaces in order to find the ones where the DR lesions are easier to detect, and then merge the information generated after the processing step. With the objective of reducing the correlation that exists among the anatomical structures in the G channel, we will also consider the work by [28], where the authors apply the PCA algorithm to generate an ad-hoc color space for their processing algorithm. This new color space could further decrease image processing complexity and improve the results. We will also investigate the merging procedure, since in this work we use a simple AND operation. Blood vessel segmentation will also be considered given the results we have obtained so far. Finally, we will also enhance the method to detect the remaining DR lesions in order to be able to generate a full diagnosis of a patient's retinopathy status.

Funding. Spanish Ministerio de Economía y Competitividad: projects ViSelTR (TIN2012-39279) and cDrone (TIN2013-45920-R). Spanish Ministerio de Educación, Cultura y Deporte: grants Salvador de Madariaga (PRX14/00614) and José Castillejo (CAS14/00238). FP7-ICT-2011-7 COMMODITY12 (287841).

Acknowledgements. We thank Ulrich Schaechtle for early discussions in the DR domain.

References

1. H. R. Taylor and J. E. Keeffe, 'World blindness: a 21st century perspective.', *Br. J. Ophthalmol.*, vol. 85, no. 3, pp. 261–266, 2001.
2. N. Cheung, P. Mitchell, and T. Y. Wong, 'Diabetic retinopathy', *Lancet*, vol. 376, no. 9735, pp. 124–136, 2010.
3. R. J. Winder, P. J. Morrow, I. N. McRitchie, J. R. Bailie, and P. M. Hart, 'Algorithms for digital image processing in diabetic retinopathy', *Comput. Med. Imaging Graph.*, vol. 33, no. 8, pp. 608–622, 2009.
4. R. Welikala, J. Dehmeshki, A. Hoppe, V. Tah, S. Mann, T. Williamson, and S. Barman, 'Automated detection of proliferative diabetic retinopathy using a modified line operator and dual classification', *Comput. Methods Programs Biomed.*, vol. 114, no. 3, pp. 247–261, 2014.
5. S. W. Franklin and S. E. Rajan, 'Diagnosis of diabetic retinopathy by employing image processing technique to detect exudates in retinal images', *IET Image Process.*, vol. 8, no. 10, pp. 601–609, 2014.
6. N. Thomas, T. Mahesh, and K. Shunmuganathan, 'Detection and Classification of Exudates in Diabetic Retinopathy', *Int. J. Adv. Res. Comput. Sci. Manag. Stud.*, vol. 2, no. 9, pp. 296–305, 2014.
7. X. Zhang, G. Thibault, E. Decencière, B. Marcotegui, B. Laÿ, R. Danno, G. Cazuguel, G. Quellec, M. Lamard, P. Massin, A. Chabouis, Z. Victor, and A. Erginay, 'Exudate detection in color retinal images for mass screening

of diabetic retinopathy', *Med. Image Anal.*, vol. 18, no. 7, pp. 1026–1043, 2014.
8. H. F. Jelinek, M. J. Cree, J. J. G. Leandro, J. V. B. Soares, R. M. Cesar, and A. Luckie, 'Automated segmentation of retinal blood vessels and identification of proliferative diabetic retinopathy', *J. Opt. Soc. Am. A*, vol. 24, no. 5, pp. 1448–1456, 2007.
9. A. Sopharak, B. Uyyanonvara, and S. Barman, 'Simple hybrid method for fine microaneurysm detection from non-dilated diabetic retinopathy retinal images', *Comput. Med. Imaging Graph.*, vol. 37, no. 5–6, pp. 394–402, 2013.
10. L. Tang, M. Niemeijer, J. M. Reinhardt, M. K. Garvin, and M. D. Abramoff, 'Splat feature classification with application to retinal hemorrhage detection in fundus images', *IEEE Trans. Med. Imaging*, vol. 32, no. 2, pp. 364–375, 2013.
11. R. Casanova, S. Saldana, E. Y. Chew, R. P. Danis, C. M. Greven, and W. T. Ambrosius, 'Application of random forests methods to diabetic retinopathy classification analyses', *PLoS One*, vol. 9, no. 6, pp. 1–8, 2014.
12. H. L. Tang, J. Goh, T. Peto, B. W. K. Ling, L. I. Al turk, Y. Hu, S. Wang, and G. M. Saleh, 'The Reading of Components of Diabetic Retinopathy: An Evolutionary Approach for Filtering Normal Digital Fundus Imaging in Screening and Population Based Studies', *PLoS One*, vol. 8, no. 7, 2013.
13. S. Roychowdhury, D. Koozekanani, and K. Parhi, 'DREAM: Diabetic Retinopathy Analysis using Machine Learning', *Biomed. Heal. Informatics, IEEE J.*, vol. 18, no. 5, pp. 1717-1728, 2014.
14. Joint ISO/CIE Standard, 'L*a*b* Colour Space. ISO 11664-4:2008(E)/CIE S 014-4/E:2007', https://www.iso.org/obp/ui/#iso:std:iso:11664:-4:ed-1:v1:en, 2008.
15. M. Niemeijer, B. Van Ginneken, J. Staal, M. S. a Suttorp-Schulten, and M. D. Abràmoff, 'Automatic detection of red lesions in digital color fundus photographs', *IEEE Trans. Med. Imaging*, vol. 24, no. 5, pp. 584–592, 2005.
16. E. Decencière, X. Zhang, G. Cazuguel, B. Lay, B. Cochener, C. Trone, P. Gain, R. Ordonez, P. Massin, A. Erginay, B. Charton, and J.-C. Klein, 'Feedback on a Publicly Distributed Image Database: the Messidor Database', *Image Anal. Stereol.*, vol. 33, no. 3, pp. 231–234, 2014.
17. M. Unser, 'Texture classification and segmentation using wavelet frames', *Image Process. IEEE Trans.*, vol. 4, no. 11, pp. 1549-1560, 1995.
18. A. Laine and J. Fan, 'Texture classification by wavelet package signatures', *IEEE Trans. Pattern Anal. Mach. Intell.*, vol. 15, no. 11, pp. 1186–1191, 1993.
19. G. Quellec, M. Lamard, P. M. Josselin, G. Cazuguel, B. Cochener, and C. Roux, 'Optimal wavelet transform for the detection of microaneurysms in retina photographs.', *IEEE Trans. Med. Imaging*, vol. 27, no. 9, pp. 1230–1241, 2008.
20. R. C. Gonzalez and R. E. Woods, *Digital Image Processing*. Prentice Hall, 2007.
21. M. Sezgin and B. Sankur, 'Selection of thresholding methods for non-desctructive testing applications', in *Image Processing*, IEEE, 2001, vol. 3, pp. 764–767.
22. J. Lim, *Two-Dimensional Signal and Image Processing*. Prentice Hall, 1989.
23. A. Gavlasová, A. Procházka, and M. Mudrová, 'Wavelet Use for Image Classification', *15th Int. Conf. Process Control. Štrbské Pleso*, Slovak University of Technology, 2005.
24. G. Lambert and F. Bock, 'Wavelet methods for texture defect detection', *Proc. Int. Conf. Image Process.*, IEEE Compt. Soc., vol. 3, pp. 201–204, 1997.
25. S. G. Mallat, 'A theory for multiresolution signal decomposition: the wavelet representation', *IEEE Trans. Pattern Anal. Mach. Intell.*, vol. 11, no. 7, pp. 674–693, 1989.
26. K. H. Ghazali, M. F. Mansor, M. M. Mustafa, and A. Hussain, 'Feature Extraction Technique using Discrete Wavelet Transform for Image Classification', in *2007 5th Student Conference on Research and Development*, IEEE, 2007, pp. 1–4.
27. R. M. Haralick, 'Statistical and structural approaches to texture', *Proc. IEEE*, vol. 67, no. 5, pp. 786–804, May 1979.
28. C. Liu, 'Learning the uncorrelated, independent, and discriminating color spaces for face recognition', *IEEE Trans. Inf. Forensics Secur.*, vol. 3, no. 2, pp. 213–222, 2008.